Airborne Measurements of Coastal Jet Transition around Point Conception, California

DAVID A. RAHN

Atmospheric Science Program, Department of Geography, University of Kansas, Lawrence, Kansas

THOMAS R. PARISH AND DAVID LEON

Department of Atmospheric Science, University of Wyoming, Laramie, Wyoming

ABSTRACT

Low-level winds along the Californian coast during spring and early summer are typically strong and contained within the cool, well-mixed marine boundary layer (MBL). A temperature inversion separates the MBL from the warmer free troposphere. This setup is often represented by a two-layer shallow-water system with a lateral boundary. Near a prominent point such as Point Conception, California, the fast-moving MBL flow is supercritical and can exhibit distinct features including a compression bulge and an expansion fan. Measurements from the University of Wyoming King Air research aircraft on 19 May 2012 during the Precision Atmospheric MBL Experiment (PreAMBLE) captured wind in excess of $14\,\mathrm{m\,s}^{-1}$ off of Point Conception under clear skies and wind $\sim 2\,\mathrm{m\,s}^{-1}$ east of San Miguel in the California Bight. A compression bulge was identified upwind of Point Conception. When the flow rounds the point, the MBL undergoes a near collapse and there is a spike in MBL height embedded in the general decrease of MBL height with greater turbulence just downwind that is associated with greater mixing through the inversion layer. Lidar and in situ measurements reveal that transport of continental aerosol is present near the pronounced MBL height change and that there is a complex vertical structure within the Santa Barbara Channel. Horizontal pressure gradients are obtained by measuring the slope of an isobaric surface. Observations of wind and pressure perturbations are able to be linked through a simple Bernoulli relationship. Variation of MBL depth explains most, but not all of the variation of the isobaric surface.

1. Introduction

Strong, low-level northerly winds are common along the California coast during spring and early summer. The equatorward flow is set up by the contrast between the broad Pacific high and the thermal low over the desert southwest. Surface wind along the coast is particularly important because it impacts the biological production in the ocean since an equatorward wind stress fosters offshore Ekman transport and coastal upwelling that brings up nutrient-rich water from below. The maximum wind speed occurs at the top of a cool, moist marine boundary layer (MBL) where a marked subsidence inversion separates the well-mixed MBL from the warm and dry free troposphere aloft. Flow in

the MBL is bounded to the east by the coastal topography that is generally above the top of the MBL. Given the stark contrast between the MBL and free troposphere, the fluid system along the coast is often represented as a two-layer shallow-water model with a lateral boundary (e.g., Winant et al. 1988; Burk et al. 1999; Dorman and Winant 2000; Dorman and Koračin 2008). Working within the hydraulic framework, fluid-flow characteristics may be understood, quantified, and compared to analogous or idealized numerical or laboratory experiments. This framework has been applied repeatedly to the flow along the west coast of California.

For a two-layer system with a lateral boundary that changes its direction (e.g., points and capes along the coastline), the Froude number Fr is an important parameter that determines whether certain hydraulic features can manifest within a layer of depth H (Dorman and Koračin 2008). In the context of coastal flow, Fr is defined as the ratio of the layer speed U to the fastest possible gravity wave in that layer ($\sqrt{g'H}$):

Corresponding author address: David A. Rahn, Atmospheric Science Program, Department of Geography, University of Kansas, 1475 Jayhawk Blvd., 201 Lindley Hall, Lawrence, KS 66045-7613.
E-mail: darahn@ku.edu

$$\mathrm{Fr} = \frac{U}{\sqrt{g'H}}, \quad \text{where} \qquad (1)$$

$$g' = g\frac{\theta_t - \theta}{\theta}. \qquad (2)$$

The reduced gravity g' is defined using the acceleration of gravity g, the layer potential temperature θ, and the potential temperature of the inversion top θ_t. Subcritical flow ($\mathrm{Fr} < 1$) moves slowly within a deep MBL. Gravity waves can propagate in any direction and redistribute the mass and wind field under subcritical conditions, allowing these fields to adjust and relax any sharp gradients. Discontinuities may arise in supercritical flow ($\mathrm{Fr} > 1$) where the flow interacts with directional changes in the lateral boundary. The flow adjusts to the change in the lateral boundary, but because gravity waves that normally redistribute the mass and wind field cannot propagate upstream, the area upstream cannot readily adjust to the change in the lateral boundary so abrupt changes may arise. Supercritical flow often exhibits marked features such as an expansion fan or an oblique hydraulic jump (sometimes referred to as shock features). Flow that is moving fast within a shallow MBL, which is typically the case along the Californian coast during spring, often demonstrates these distinctive hydraulic features. Burk and Haack (2000) examined wave clouds upwind of coastal orography. Burk and Thompson (2004) show an example of an impressive succession of shock wave clouds in the transcritical region between strong northerly flow and a southerly surge.

A range of numerical simulations have been conducted to explore the fluid system. Idealized simulations such as Edwards et al. (2001) have simplified coastlines and imposed pressure gradients acting on a shallow layer of fluid under an inactive deep layer. Söderberg and Tjernström (2001) also use different terrain configurations in idealized simulations to examine topographic influences. Haack et al. (2001) use a combination of an idealized and a more realistic simulation to investigate the MBL response to a change in the coastline. These studies reveal that models are able to realistically capture how the depth of the MBL, including any hydraulic jumps, and the wind speed is modified by the coastline under different conditions. There is a lack of measurements that show the finescale structure of the actual MBL and wind field when there are sharp changes in coastline. Pertinent variables include how much the MBL depth decreases in an expansion fan, what the horizontal scale of the transition is, and how quickly the wind responds to changes in the MBL height.

Response of the MBL near an extreme bend in the coastline during June was simulated by Dorman and Koračin (2008), which also included many observations in the region. Several causes were investigated and it was concluded that atmospheric marine layer hydraulic dynamics were the dominant factor in controlling the system given favorable synoptic conditions. Other factors such as diurnal heating and the land/sea breeze may have a strong influence. The potential temperature difference across the MBL top was also viewed as critical since energy is trapped within the MBL instead of escaping upward. Aircraft observations of this transition during a relatively "ideal" synoptic setting are presented here for the 19 May 2012 case. The ideal synoptic setting is considered to be westerly flow or at most a weak easterly flow in the Santa Barbara Channel. Nonideal conditions are any situations that could significantly alter the transition of the flow around Point Conception, California (e.g., a Catalina eddy or a southerly surge). Airborne measurements have been taken that reveal the finescale details of the transition about the Point Conception headland including how the inversion layer responds. Data and methods are introduced in section 2. Results are presented in section 3 and focus on a flight from 1800 to 2100 UTC 19 May 2012. A summary of the findings and their implications is discussed in section 4.

2. Data

Measurements were obtained during the Precision Atmospheric MBL Experiment (PreAMBLE) based out of Point Mugu, California, from 15 May to 17 June 2012. The primary observational platform was the University of Wyoming King Air (UWKA), which can detect finescale vertical structure offshore and precisely map the horizontal pressure gradient force (PGF) by flying on an isobaric surface and determining the slope of the height field. Independent isobaric height measurements have traditionally been taken by radar altimeters, but more recently differential global positioning system (GPS) processing has been used and provides a more accurate measurement. The height of an isobaric surface needs to be known to within a fraction of a meter to enable calculation of the PGF. For example, a $10 \, \mathrm{m \, s^{-1}}$ geostrophic wind at 43°N is associated with an isobaric height change of 10 cm every kilometer. Any deviation of the aircraft autopilot off the isobaric surface is corrected with the hypsometric equation that requires an accurate static pressure measurement. This technique has been proven in previous cases (e.g., Rahn and Parish 2007) and details can be found in Parish et al. (2007) and Parish and Leon (2013). To apply the technique, any pressure tendency during the flight must be known since it would alter the relative slope. Simply flying reciprocal
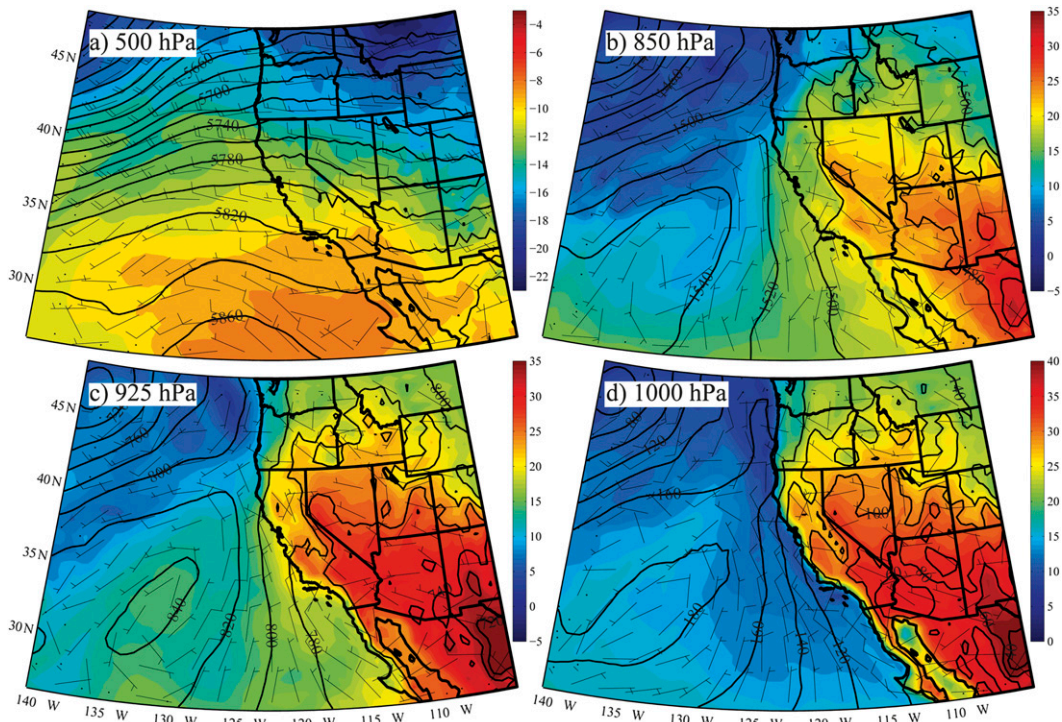
FIG. 1. Isobaric maps at 1800 UTC 19 May 2012 depicting height (m, contours), temperature (°C, color scale), and wind barbs (m s^{-1}) at (a) 500, (b) 850, (c) 925, and (d) 1000 hPa. Data are from the 0.5° resolution of the Climate Forecast System, version 2, that is run with 64 vertical levels (Saha et al. 2010).

legs alleviates the problem of pressure tendencies since repeating the same leg in the opposite direction reveals any time tendency.

The Wyoming Cloud Lidar (WCL) was on board the UWKA during PreAMBLE and was configured with upward- and downward-looking beams. The WCL is a 355-nm lidar designed for retrieval of cloud and aerosol properties. The returned signal for the upward-looking lidar is sampled at 3.75-m intervals, while the returned signal for the downward looking lidar is sampled at 1.5-m intervals. Additional details of the WCL can be found in Wang et al. (2009) and Wang et al. (2012). The lidar data are combined with the aircraft's inertial navigation system and GPS data from the UWKA to produce time–height images of the (uncalibrated) attenuated backscatter. The lidar is well suited to determine cloud boundaries, but because the lidar signal is rapidly attenuated in cloud, the lidars are unable to penetrate deeply into the cloud layer. Lidar data have been collected in the past during Coastal Waves 1996 (Rogers et al. 1998); however, an important advancement is the depolarization ratio (the ratio of perpendicular to parallel polarized backscattered radiation intensity), which assisted in the physical interpretation of the transition region.

3. Results

a. General conditions

At 1800 UTC 19 May 2012, California was under a broad ridge at 500 hPa (Fig. 1). Relatively warm temperatures extend down underneath the ridge to 925 hPa where the low-level anticyclone is clearly situated southwest of California. A strong PGF was present to drive the northerly wind along the coast. Cyclonic vorticity exists to the south of Point Conception as a result of horizontal wind shear, yet little evidence in the reanalysis is found of southerly flow along the coast or a well-defined Catalina eddy. Satellite imagery (not shown) does depict weak southerly flow and low clouds reaching Santa Cruz, California, in the early morning before retracting south during the day. Cyclonic circulations were prevalent in the California Bight throughout the PreAMBLE field study, but on this day such circulation features were relatively weak. Leeward conditions are considered important in the adjustment process as the northerly flow west of Point Conception reaches the Santa Barbara Channel. A case during PreAMBLE with strong northerly wind encountering a strong southerly flow in the lee of Point Conception will be discussed in a subsequent paper. For the 19 May 2012 case,
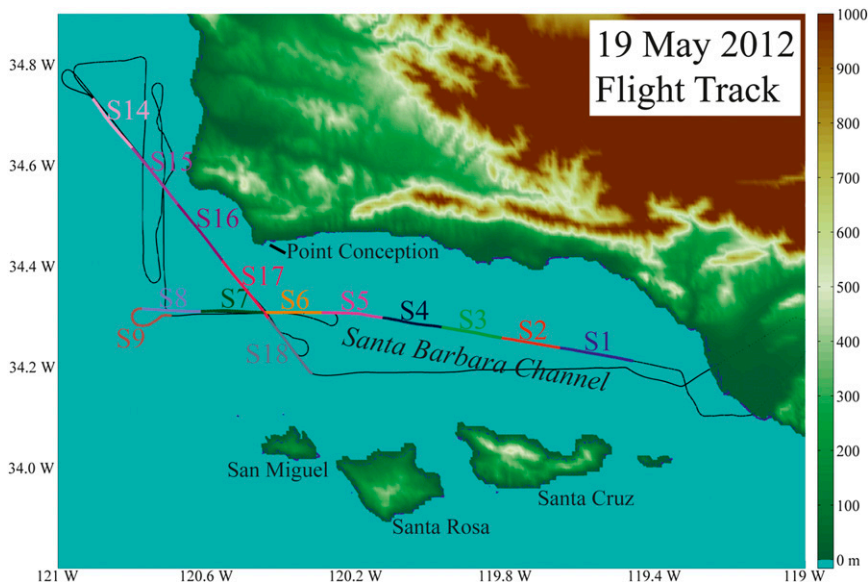
FIG. 2. Topographic elevation (m) and flight track on 19 May 2012. Location of each sounding overlaid on the flight track.

temperatures at 1000 hPa were cooler than 925 hPa, reflecting the cool MBL below the warm, dry subsiding air. Only some fog/low cloud was present right at Point Conception in the morning, but dissipated after sunrise. The UWKA flight was conducted in clear skies. Buoy coastal observations near Point Conception reveal northwesterly winds between 8 and 12 m s^{-1} throughout the day on 19 May. Surface wind near Santa Barbara had an easterly component until 1200 UTC when the wind direction changed to westerly.

The flight strategy on this day focused on the transition of the flow as it passed around Point Conception (Fig. 2). Three sets of legs were conducted. Each consisted of two isobaric legs (flown at ~990 hPa) and a series of vertical sawtooth maneuvers in which the aircraft sampled the MBL from about 100 to 900 m above the ocean. The legs were centered on Point Conception and orientated zonally, meridionally, and along a northwest–southeast track. Data taken while the aircraft is not on a straight flight path (banking) are not plotted. The discussion focuses on the upwind, downwind, and the transition of the flow around the cape by highlighting the pertinent flight legs and synthesizing them at the end.

b. Meridional legs and upwind conditions

A set of redundant isobaric legs directed from south to north and back south was conducted to measure the isobaric height and thus the meridional PGF (Fig. 3). The returning isobaric leg from north to south deviated from the original flight track by avoiding helicopter traffic from a nearby oilrig platform and the subsequent

vertical sawtooth profiling leg returning north was shifted westward. Despite this deviation, the height of the isobaric surface in the northern portion was nearly the same for both of the legs. In contrast, larger differences in the isobaric height between the reciprocal legs were observed near the southern end. A wavelike structure was present that may be shifting slowly over time. Wind speed increases from 11 to 14 m s^{-1} toward the south. During these legs the aircraft was within the MBL as inferred from the high relative humidity and lidar (not shown).

From previous conceptual models of hydraulic flow (e.g., Dorman and Koračin 2008), key features can be identified. The upstream Fr is about 0.9, which is calculated from sounding 14 where $\theta = 285$ K, $\theta_t = 298$ K, $U = 10$ m s^{-1}, and $H = 300$ m. Strictly speaking, Fr of unity is transcritical. The calculation and meaning of Fr is imprecise in the real atmosphere because of departures from shallow-water theory. The ideal case is a homogeneous, single-layer fluid, while the atmosphere is variably stratified. However, it is the relative numbers that are important (Burk and Thompson 2004). For example, Dorman and Koračin (2008) define transcritical and supercritical as Fr > 0.5. So, north of Point Conception a Froude number of 0.9 suggests a supercritical environment, which allows hydraulic features to manifest in the flow. An isobaric height maximum is found 15 km south of the northernmost point of the leg, indicating higher surface pressure and a deeper MBL that is associated with a compression bulge. The meridional wind is the weakest from the beginning of the leg to
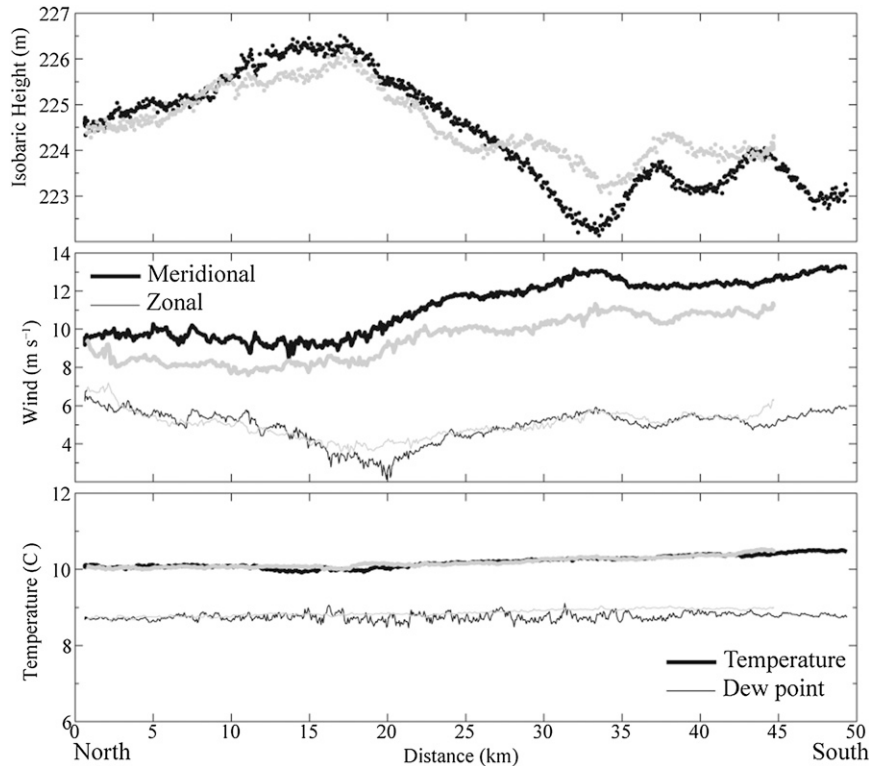
FIG. 3. In situ aircraft data for the north–south isobaric flight legs. Black is used for the first leg and gray for the returning leg. (top) Corrected isobaric height (m), (middle) negative meridional wind component (m s^{-1}, thick) and zonal wind component (m s^{-1}, thin), and (bottom) temperature (°C, thick) and dewpoint temperature (°C, thin). Time of legs is 1858–1919 UTC.

a distance of 15 km. Isobaric height decreases abruptly southward until the wavelike features. As the isobaric height drops ~3 m over 15 km, the meridional wind speed increases ~3 m s^{-1}.

c. Zonal legs and downwind conditions

While the meridional legs were flown entirely within the MBL, the zonal legs (Fig. 4) reveal that the MBL continues to thin to the east. Just 10 km east of the southernmost part of the meridional legs, the aircraft (flying ~220 m) exits the downward-sloping MBL and enters the warmer and drier air just above the MBL where the wind decreases. At the westernmost point of the zonal legs the isobaric height again reveals a wavelike structure near the top of the MBL that is repeated in both legs. The waves are sampled 17 min apart and the redundancy of the observed wave features attests to the near-stationarity of the height field. As the plane flies from west to east the temperature and dewpoint clearly indicate that the plane is entering the warmer and drier free troposphere east of the 12-km distance in Fig. 4. Interestingly, to the east the dewpoint increases to values greater than in the MBL, which suggests an absence of

large-scale subsidence above the MBL and a departure from the classic MBL structure to the west of the California coast (e.g., Rahn and Parish 2007).

d. Northwest–southeast legs and transition characteristics

The northwest–southeast legs are directed along an axis parallel to the mean wind to capture the transition about the coastal headland of Point Conception. Traditional interpretation of hydraulic features along the coast includes a compression bulge upwind of a coastal point and an expansion fan downwind. UWKA observations (Fig. 5) from this case indicate that a compression bulge is present. The isobaric surfaces have higher heights in a 40-km bulge north of the point. Heights drop abruptly at ~45 km where a sharp spike in the isobaric height is detected. This spike is not only present in the isobaric surface, but is also evident in the wind. This MBL near collapse shows some difference from a classic expansion fan that will be discussed later.

Parish and Oolman (2012) demonstrated the relationship between the wind and isobaric height perturbations measured by the UWKA under the extreme
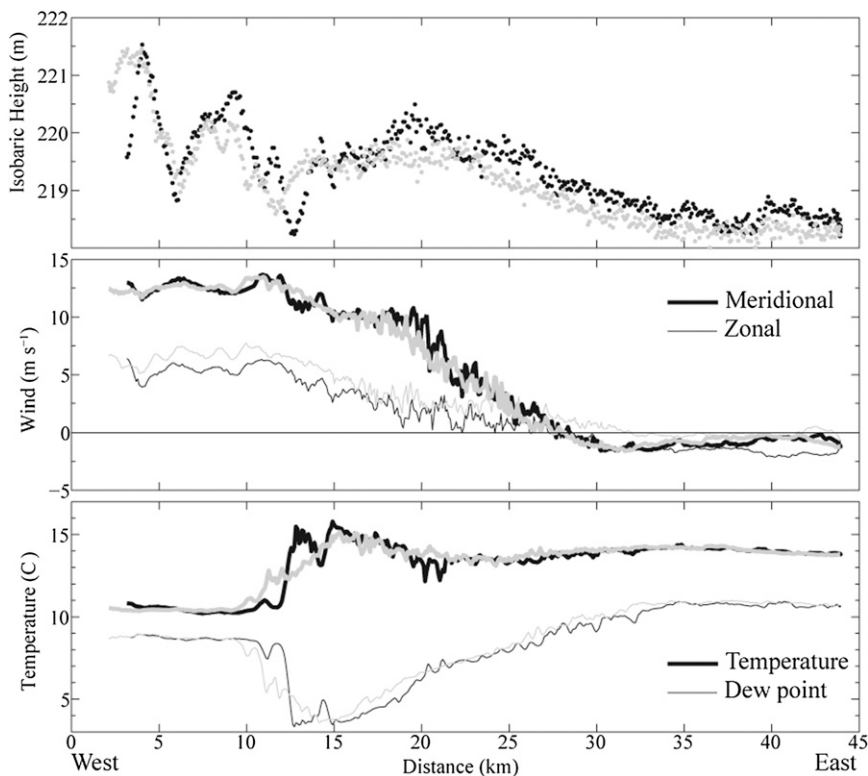
FIG. 4. As in Fig. 3, but for the west–east isobaric leg. Time of legs is 1840–1858 UTC.

conditions of mountain waves in the lee of the Sierra Nevada during the Terrain-Induced Rotor Experiment (T-REX; Grubišić et al. 2008). Isobaric height perturbations as much as 70 m over 10–15 km were detected with along-flight wind changes of 15 m s^{-1}. They showed that the wind responded directly to the horizontal PGF as an idealized Bernoulli flow, similar to Smith et al. (2008). The waves near Point Conception are much less dramatic than the waves induced by the Sierra Nevada, but the precise measurements allow these features to be examined. A closer view of these waves (Fig. 6) reveals perturbations on the order of 2–2.5 m in the isobaric height and 3–3.5 m s^{-1} in the wind magnitude over 1 km. They are negatively correlated so that an increase of height corresponds to lower wind speed. From Eq. (3) the inviscid momentum equation for motion in isobaric coordinates along an axis x (defined here along the flight track) and assuming that the system is in steady state, Coriolis is small over the scale of the perturbation, advection of cross-leg wind is small, and vertical advection is small compared to the horizontal pressure gradient, the equation reduces to Eq. (4). Integrate the remaining terms in Eq. (4) to arrive at Eq. (5), which contains the key components in the atmospheric Bernoulli equation:

$$\frac{\partial u}{\partial t} + u\frac{\partial u}{\partial x} + v\frac{\partial u}{\partial y} + \omega\frac{\partial u}{\partial p} = -g\frac{\partial z}{\partial x} + fv, \qquad (3)$$

$$u\frac{\partial u}{\partial x} = -g\frac{\partial z}{\partial x}, \qquad (4)$$

$$\frac{u^2}{2} + gz = C_o. \qquad (5)$$

Equation (5) is applied to the aircraft measurements to calculate the wind speed perturbations from the changes in isobaric height and vice versa (Fig. 6). For the first leg, the Bernoulli equation explains the connection between wind and isobaric height with only slight errors in the vicinity of the large wave. When the aircraft is just east of the large wavelike perturbation, the aircraft is out of the MBL, so the relationship between MBL depth and wind speed is no longer applicable. The only discrepancy in the second leg is near 45.25 km where a short increase of wind is not reflected in the isobaric surface. The reason why is not clear. About 18 min separate these measurements. However, the minimum in wind speed at 46 km is well represented by the Bernoulli equation. Even though the perturbations to height and wind speed are relatively small compared to much greater perturbations seen in
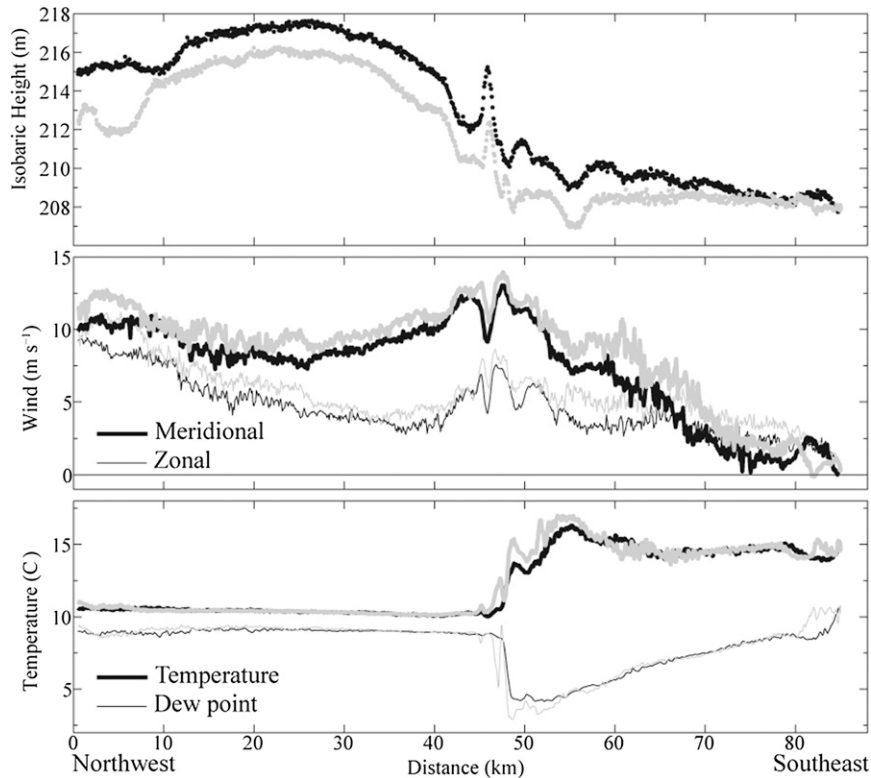
FIG. 5. As in Fig. 3, but for the northwest–southeast isobaric leg. Time of legs is 1934–2009 UTC.

mountain waves, the measurements are able to detect these changes over just a couple of kilometers and directly link the isobaric height and wind speed. The inverse relationship is also present under the compression bulge where the wind decreases under the higher isobaric height.

The aircraft is in the cool, humid MBL in the northwest part of the leg and at ~50 km the temperature increases sharply while the dewpoint drops below 5°C. Just east of the wave features the UWKA is flying through the inversion layer at the top of the MBL. Toward the southeast the temperature above the inversion remains fairly constant, but the dewpoint increases slowly into the Santa Barbara Channel, consistent with the zonal leg (Fig. 4).

Since the UWKA is above the MBL in the southeast portion of the leg, in situ data do not reveal characteristics of an expansion fan. The lidar on board the UWKA is able to remotely detect changes of the lower atmosphere, especially MBL depth. In clear air the lidar differentiates between the MBL and the free troposphere due to the gradient in aerosol. Consistent with in situ measurements within the MBL, the upward-pointing lidar detected changes in the MBL height (Fig. 7). Upstream of the wave features the MBL is deeper and

associated with the compression bulge. Above the wavelike perturbation in isobaric height there is a large, well-defined spike in MBL height. The MBL height changes approximately 100 m from the top of the spike to the shallowest MBL height to the northwest.

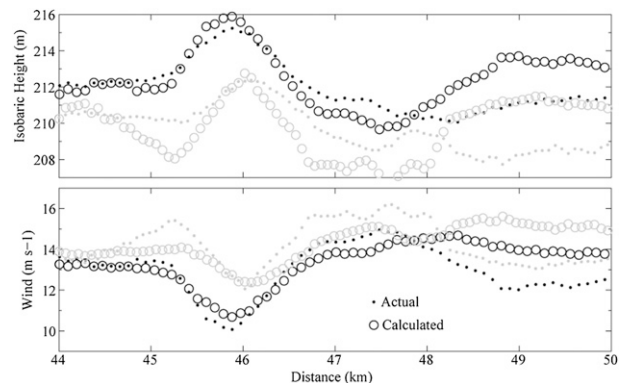Using the lidar returns, the height of the MBL may be quantified (Fig. 8). As evident in Fig. 7, the top of the

FIG. 6. Magnified view of Fig. 5 depicting the (top) isobaric height (m) and (bottom) wind speed (m s^{-1}). The actual measurements are the dots while the circles are the calculated changes based off of the other value (see text).
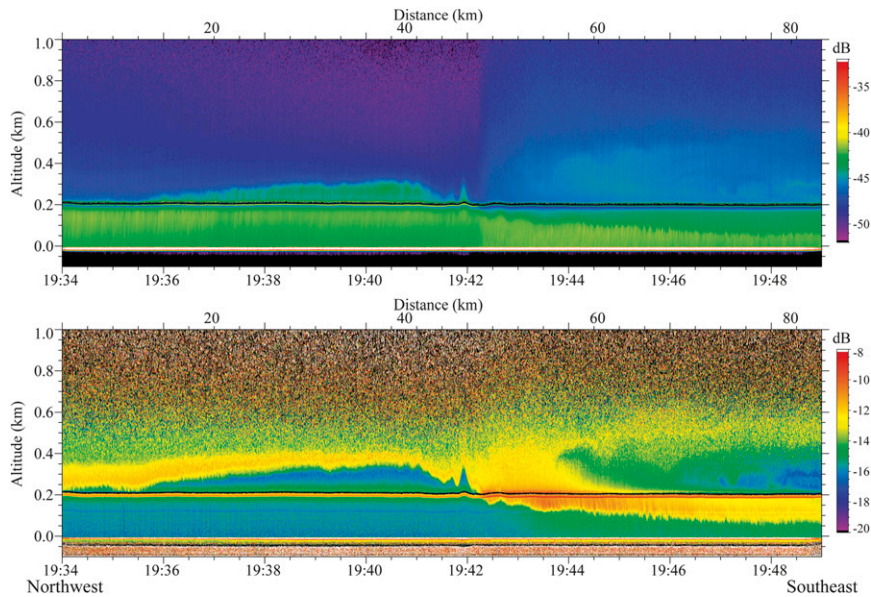
FIG. 7. Lidar returns of (top) reflectivity (dB) and (bottom) depolarization (dB) for the first leg in Fig. 5.

MBL is marked by a pronounced decrease in the attenuated backscatter collocated with an increase in the depolarization ratio. Quantitatively, MBL height is defined as the lowest altitude where the WCL power is less than a set threshold (chosen here to be −2 dB) and the depolarization ratio exceeds a threshold (chosen here to be −6 dB). Variation in the MBL height associated with

the compression bulge, expansion fan, and the large spike are all readily detected. Since changes in the depth of the MBL can be related to the underlying pressure using the hypsometric equation (e.g., Dorman 1987), the MBL heights derived from the lidar may be used to calculate the expected change in isobaric height. From the soundings along the northwest to southeast flight
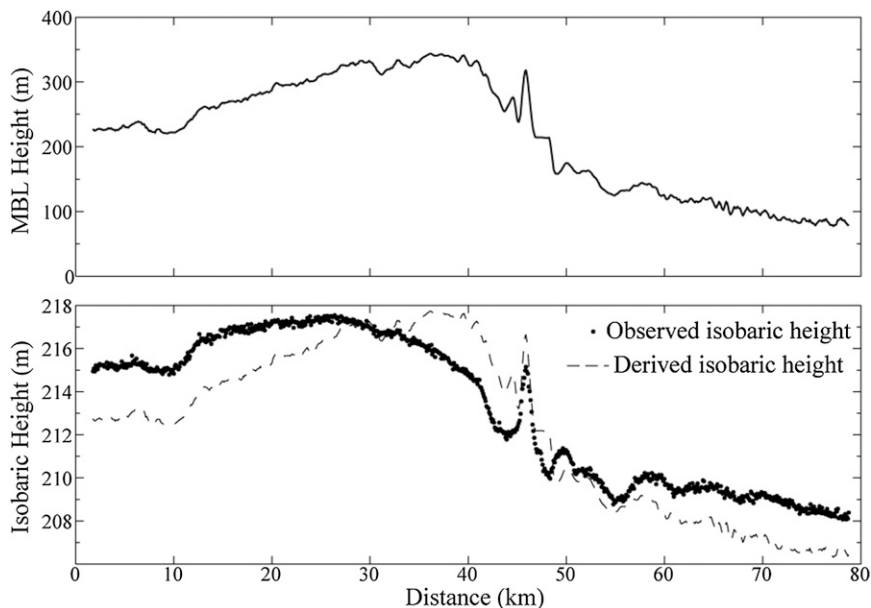

FIG. 8. For the first leg of Fig. 5 and the lidar image in Fig. 7 the (top) MBL height (m) derived from the lidar, and (bottom) isobaric surface from the in situ aircraft measurements (m, points) and isobaric surface derived from the MBL height (m, dashed line).
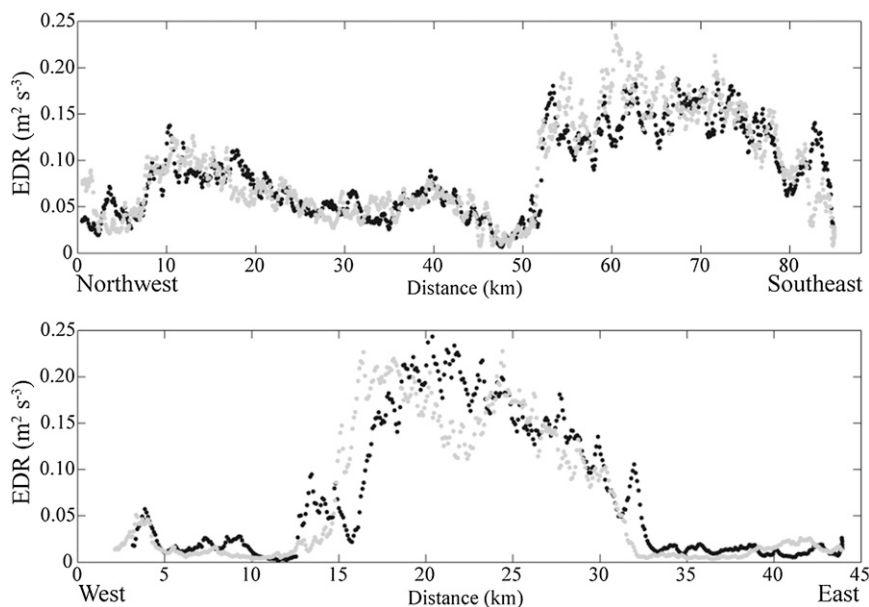
FIG. 9. EDR ($m^2 s^{-3}$) from the MRI sensor for the (top) northwest–southeast depicted in Fig. 5 using the same scale and (bottom) west–east isobaric leg depicted in Fig. 4 using the same scale.

path, a temperature jump of 10°C is assumed. Comparing the observed isobaric height and the derived isobaric height, they have the same general structure and also have the same small-scale undulations such as that around 10 km and the spike at 45 km. A notable difference is that the observed isobaric height flattens at about 25 km and begins to decrease while the derived isobaric height continues to increase until 40 km before dropping sharply. The reason for the difference between the derived and observed isobaric height is not entirely clear, but it is likely related to the assumption of the derived heights that the jump in temperature across the inversion is constant or that there is a concomitant change in the temperature gradient aloft that is not going to be picked up in the simple MBL height and pressure relationship.

Just downstream of the largest spike of the MBL height the reflectivity does not indicate any strong features above the MBL, but the depolarization reveals the impact of the wave downstream of the jump. Depolarization represents the irregularity of the backscattered radiation. If the surface of the aerosol is irregularly shaped, the returned radiation will be depolarized. If the object is more uniform, such as that for deliquesced aerosol, then the lidar return will also be more uniform and hence the returned signal has a low ratio. Instrumentation on board the UWKA includes a passive cavity aerosol spectrometer probe (PCASP) that is able to detect aerosol with diameters greater than

about $0.1 \, \mu$m (Cai et al. 2013). PCASP total concentration measurements for the leg shown in Fig. 7 within the MBL were typically about $250 \, cm^{-3}$. As the UWKA moved across the MBL boundary, PCASP total concentration increased to nearly $400 \, cm^{-3}$. This change in concentration to a high number of dry, irregularly shaped aerosols with a high depolarization ratio is consistent with that of a continental air mass. Thus, the high depolarization ratios depicted east of the large wave activity at the top of the MBL are interpreted as aerosol that has been advected off the continent. Such a transport represents a departure from standard hydraulic theory that assumes a rigid lateral boundary and a passive upper layer. Further, the advection of warm, dry air off the continent is consistent with the observed isobaric height gradient that shows a marked change at the boundary where continental effects are observed. However, it is difficult to separate the influence of the offshore flow from dynamics associated with an expansion fan.

Evidence of an increased entrainment and turbulence is indicated by the eddy dissipation rate (EDR) in Fig. 9. EDR is measured by the Meteorology Research Incorporated (MRI) turbulence sensor using the method developed by MacCready (1964). More turbulence (higher EDR) is seen in the northwest–southeast and zonal legs just downwind of the wave features and in the area of highest depolarization. After the maximum in EDR, it decreases east into the Santa Barbara Channel. The large EDR is consistent with the lidar returns since the
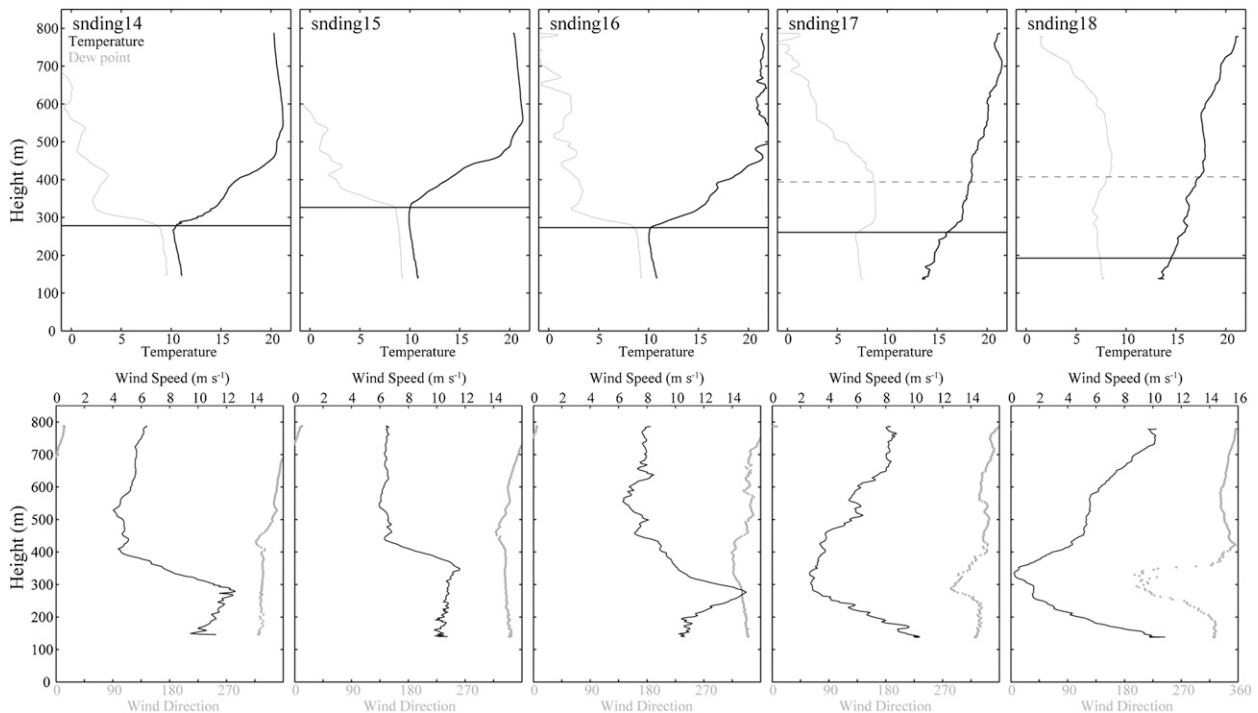
FIG. 10. Soundings taken along the northwest–southeast track (location in Fig. 2) showing (top) temperature (black, °C) and dewpoint temperature (gray, °C) and (bottom) wind speed (black, m s^{-1}) and wind direction (°, gray).

depolarization has a maximum where there is some off-shore flow and right after the large wave activity. The EDR decreases toward the east away from these features. Enhanced turbulence as the MBL collapses is associated with more mixing at the MBL top and can change the layer properties, as will be shown by the soundings.

In the southeast the lidar indicates some hint of another layer above the aircraft, although it is weak. A robust two-layer assumption for the MBL is only observed in the profiles at the entrance of the Santa Barbara Channel. Soundings from the sawtooth along the northwest–southeast flight track (Fig. 10) show that in the farthest northwest section (sounding 14) the classic and well-defined, cool, moist MBL is present with a subsidence inversion of about 10°C over 200 m and a drop in dewpoint temperature that separates the MBL and free troposphere. The wind is out of the north-northwest with a maximum of 12 m s^{-1} at the base of the inversion. The next sounding to the southeast (sounding 15) shows the same features but with a deeper MBL associated with the compression bulge. Sounding 16 depicts an MBL that has returned to about the same height as the first sounding in this series and the wind speed has increased ~2 m s^{-1}. Note that a wind direction from the north is consistent with transport of warm air from the continent. Sounding data from the UWKA indicate off continent flow at levels above about 400 m.

The classic temperature structure begins to deviate from two clear layers represented by the MBL and free troposphere in the fourth sounding (sounding 17), which is taken just downstream of the jump. The MBL is extremely shallow (~200 m) and the temperature profile does not contain any strong localized inversions. The inversion can no longer be considered a sharp transition between the marine layer and free atmosphere. Note that the dewpoint temperature actually rises, indicating that large-scale subsidence cannot be taking place. Instead, the temperature increases with height throughout nearly the entire sounding. This is consistent with warm air transport off the continent. Wind directions above about 400 m also suggest off continent flow. The dewpoint profile suggests layers of similar moisture content. The dewpoint is ~7°C below 250 m, ~9°C between 250 and 400 m, and decreases above 400 m. Moisture content seems to be tied to the lidar returns (Fig. 7) and may reflect subtle differences in relative humidity. Changes in the wind speed and direction also support the existence of three layers. Wind in the southeastern profile (sounding 18) indicates a wind from northwest below 200 m, lighter wind speeds out of the southwest between 200 and 400 m, and stronger winds from the north above 400 m that again is evidence of flow originating over the continent.

From the isobaric legs (Figs. 4 and 5), the moisture content tends to increase slowly toward the east from the
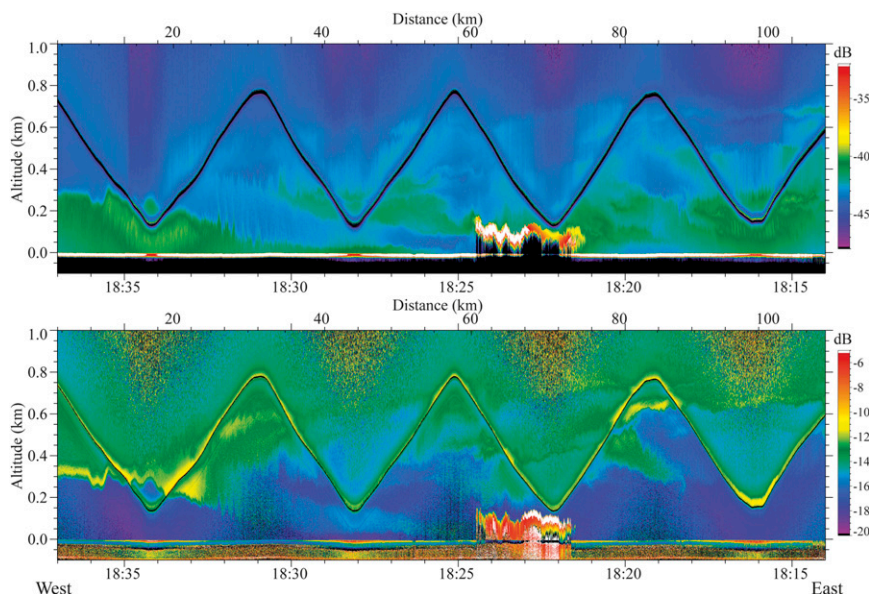
FIG. 11. As in Fig. 7, but for the zonal track within the Santa Barbara Channel (soundings 1–8).

driest region after the collapse of the MBL. Soundings along the same track confirm the trend below 700 m, especially between 300 and 400 m. Features in the Santa Barbara Channel are obtained from the lidar and a set of soundings on the way out to Point Conception from Point Mugu, California. Lidar returns (Fig. 11) and soundings (Fig. 12) during the sawtooth leg reveal a complex structure. In the west the MBL is clearly identifiable in both the reflectivity and the depolarization. The MBL top is about 300 m and slopes down from the west until essentially reaching the surface. The slope is not as steep as in Fig. 7 since the leg is not orientated directly along the MBL height gradient. Wavelike features are at

the top of the MBL, consistent with the nonlinear nature of the flow as it transitions from supercritical to subcritical. It is evident from the lidar returns that within the channel there is not one simple layer that is entirely well mixed from the surface up to the top of an inversion layer that separates the MBL from the free troposphere. In the reflectivity there appears to be several horizontal bands of higher reflectivity (also visible in the depolarization), so it is not clear if one can identify a single layer, but perhaps multiple layers.

While these features may not be strongly represented in the lidar images, in situ measurements during this leg give clues about the origin of the layers. In the east near
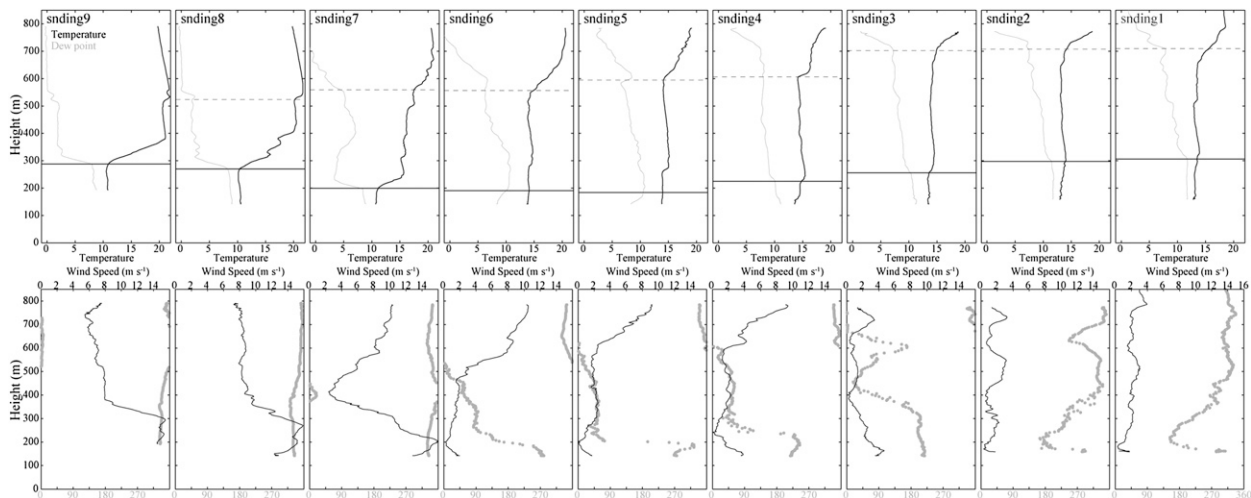

FIG. 12. As in Fig. 10, but for the zonal track within the Santa Barbara Channel (soundings 1–8).

the apex of the sawtooth patterns, the temperature and dewpoint indicate a subsidence inversion near 700 m that caps moist and cool air below. The subjectively estimated height of the subsidence inversion base is indicated by the gray dashed lines. The inversion base lowers toward the west at the same time that the vertical gradient in the temperature and dewpoint temperature is apparently weakening. There is some slight indication of a layer in soundings 8 and 9 but its identity is largely lost by this point. Underneath the weakening upper-level inversion in the west is the MBL originating from the north, which is much better defined. The height of the MBL decreases into the channel until essentially reaching the surface. Under a simple, two-layer system the MBL thins until reaching the stagnant sector, which is composed of the upper layer characteristics. In this case, an ideal two-layer system within the Santa Barbara Channel is invalid since the characteristics of the layer aloft are changing spatially, multiple layers are evident, and off-continent transport is present.

4. Summary and discussion

Flights during PreAMBLE were centered on Point Conception in the vicinity of the greatest changes in the MBL height and wind. Flight patterns consisted of isobaric flight legs and a series of ascents and descents culminating in a sawtooth flight pattern. Only a small fraction of the atmosphere is actually sampled in situ, but the lidar remotely senses a continuous cross section. The compression bulge and marked collapse of the MBL as the flow rounded Point Conception was apparent. Undulations and variations of the MBL and flow properties were also observed. These were measured with high precision and wind and pressure perturbations display a Bernoulli relationship. Sharp perturbations at the top of the MBL manifested and were fairly stationary near the pronounced MBL height change. Downwind of Point Conception and tied to the near collapse of the MBL, there is transport of continental aerosol that is inferred from the lidar depolarization and in situ UWKA measurements of number concentration.

Observations also reveal a deep layer lingering within the Santa Barbara Channel that is not as cool as that north of Point Conception, but is cooler than the free troposphere above which is separated by a weaker temperature inversion. What consequence does the relatively deep MBL in the Santa Barbara Channel have? This layer influences the flow coming from the northwest of Point Conception, but since there is a deeper layer of cool air toward the east there would have to be an associated PGF directed against the flow arriving from the north. As in Fig. 15 of Dorman and Koračin (2008),

the structure of the MBL within the Santa Barbara Channel is consistent with the pressure minimum in that region between the relatively high pressure associated with the cold, dense MBL toward the west and the deeper, cool MBL to the east farther within the California Bight. They also report that the pressure minimum is a common feature for moderate and strong wind cases.

During strong wind cases around Point Conception, cyclonic vorticity is readily observed in the California Bight and is a nearly ubiquitous feature during the spring and early summer. Cyclonic vorticity suggests that there is southerly flow and a deep MBL near the coast that is deepest toward the south with a PGF along the coast from south to north (e.g., Parish et al. 2013). Another case on 3 June with strong southerly flow more clearly illustrates the interaction between the northerly flow as it rounds Point Conception with an opposing flow coming from deeper in the Santa Barbara Channel.

This work is meant to highlight the important differences between the ideal system used in the conceptual models, which are a good first-order approximation and capture most of the essential dynamics, and the actual atmosphere to identify where the departures are from the ideal cases. Departures from the ideal include enhanced vertical mixing at the MBL collapse, a nonpassive upper layer due to offshore flow, and interaction with a deeper MBL in the Santa Barbara Channel. Other factors such as the diurnal changes in radiation, lee waves, opposing wind the Santa Barbara Channel, and sea/land breezes, will also modify the flow, but this case was the closest to ideal during the field project. While variation of the MBL depth can explain most of the changes to the underlying isobaric height field, especially the sharp wavelike perturbation, it cannot explain all of the isobaric height field changes (Fig. 8). The observations obtained with PreAMBLE may also be used to help diagnose some of these issues and identify any model deficiencies.

REFERENCES

Burk, S. D., and T. Haack, 2000: The dynamics of wave clouds upwind of coastal orography. *Mon. Wea. Rev.,* **128,** 1438–1455.

——, and W. T. Thompson, 2004: Mesoscale eddy formation and shock features associated with a coastally trapped disturbance. *Mon. Wea. Rev.,* **132,** 2204–2223.

——, T. Haack, and R. M. Samelson, 1999: Mesoscale simulation of supercritical, subcritical, and transcritical flow along coastal topography. *J. Atmos. Sci.,* **56,** 2780–2795.

Cai, Y., J. R. Snider, and P. Wechsler, 2013: Calibration of the passive cavity aerosol spectrometer probe for airborne determination of the size distribution. *Atmos. Meas. Tech. Discuss.,* **6,** 1–29.

Dorman, C. E., 1987: Possible role of gravity currents in northern California's coastal summer wind reversals. *J. Geophys. Res.,* **92** (C2), 1497–1506.

——, and C. D. Winant, 2000: The structure and variability of the marine atmosphere around the Santa Barbara Channel. *Mon. Wea. Rev.,* **128,** 261–282.

——, and D. Koračin, 2008: Response of the summer marine layer flow to an extreme California coastal bend. *Mon. Wea. Rev.,* **136,** 2894–2992.

Edwards, K. A., A. M. Rogerson, C. D. Winant, and D. P. Rogers, 2001: Adjustment of the marine atmospheric boundary layer to a coastal cape. *J. Atmos. Sci.,* **58,** 1511–1528.

Grubišić, V., and Coauthors, 2008: The Terrain-Induced Rotor Experiment: An overview of the field campaign and some highlights of special observations. *Bull. Amer. Meteor. Soc.,* **89,** 1513–1533.

Haack, T., S. D. Burk, C. Dorman, and D. Rodgers, 2001: Supercritical flow interaction within the Cape Blanco–Cape Mendocino orographic complex. *Mon. Wea. Rev.,* **129,** 688–708.

MacCready, P. B., Jr., 1964: Standardization of gustiness values from aircraft. *J. Appl. Meteor.,* **3,** 439–449.

Parish, T. R., and L. D. Oolman, 2012: Isobaric height perturbations associated with mountain waves measured by aircraft during the Terrain-Induced Rotor Experiment. *J. Atmos. Oceanic Technol.,* **29,** 1825–1834.

——, and D. Leon, 2013: Measurement of cloud perturbation pressures using an instrumented aircraft. *J. Atmos. Oceanic Technol.,* **30,** 215–229.

——, M. D. Burkhart, and A. R. Rodi, 2007: Determination of the horizontal pressure gradient force using global positioning system onboard an instrumented aircraft. *J. Atmos. Oceanic Technol.,* **24,** 521–528.

——, D. A. Rahn, and D. Leon, 2013: Airborne observations of a Catalina eddy. *Mon. Wea. Rev.,* **141,** 3300–3313.

Rahn, D. A., and T. R. Parish, 2007: Diagnosis of the forcing and structure of the coastal jet near Cape Mendocino using in situ observations and numerical simulations. *J. Appl. Meteor. Climatol.,* **46,** 1455–1468.

Rogers, D. P., and Coauthors, 1998: Highlights of Coastal Waves 1996. *Bull. Amer. Meteor. Soc.,* **79,** 1307–1326.

Saha, S., and Coauthors, 2010: The NCEP Climate Forecast System Reanalysis. *Bull. Amer. Meteor. Soc.,* **91,** 1015–1057.

Smith, R. B., B. K. Woods, J. Jensen, W. A. Cooper, J. D. Doyle, Q. Jiang, and V. Grubišić, 2008: Mountain waves entering the stratosphere. *J. Atmos. Sci.,* **65,** 2543–2562.

Söderberg, S., and M. Tjernström, 2001: Supercritical channel flow in the coastal atmospheric boundary layer: Idealized numerical simulations. *J. Geophys. Res.,* **106** (D16), 17 811–17 829.

Wang, Z., P. Wechsler, W. Kuestner, J. French, A. Rodi, B. Glover, M. Burkhart, and D. Lukens, 2009: Wyoming cloud lidar: Instrument description and applications. *Opt. Express,* **17,** 13 576–13 587.

——, and Coauthors, 2012: Single aircraft integration of remote sensing and in situ sampling for the study of cloud microphysics and dynamics. *Bull. Amer. Meteor. Soc.,* **93,** 653–668.

Winant, C. D., C. E. Dorman, C. A. Friehe, and R. C. Beardsley, 1988: The marine boundary layer off northern California: An example of supercritical channel flow. *J. Atmos. Sci.,* **45,** 3588–3605.